Multi-pass Fast Watershed for Accurate Segmentation of Overlapping Cervical Cells

Afaf Tareef*, *Student Member, IEEE,* Yang Song, *Member, IEEE,* Heng Huang, *Member, IEEE,* Dagan Feng, *Fellow, IEEE,* Mei Chen, *Member, IEEE,* Yue Wang, *Fellow, IEEE,* Weidong Cai, *Member, IEEE*

***Abstract*—The task of segmenting cell nuclei and cytoplasm in Pap smear images is one of the most challenging tasks in automated cervix cytological analysis due to specifically the presence of overlapping cells. This paper introduces a multi-pass fast watershed-based method (MPFW) to segment both nucleus and cytoplasm from large cell masses of overlapping cervical cells in three watershed passes. The first pass locates the nuclei with barrier-based watershed on the gradient-based edge map of a pre-processed image. The next pass segments the isolated, touching, and partially overlapping cells with a watershed transform adapted to the cell shape and location.**

The final pass introduces mutual iterative watersheds separately applied to each nucleus in the largely overlapping clusters to estimate the cell shape. In MPFW, the line-shaped contours of the watershed cells are deformed with ellipse fitting and contour adjustment to give a better representation of cell shapes. The performance of the proposed method has been evaluated using synthetic, real extended depth-of-field, and multi-layers cervical cytology images provided by the first and second overlapping cervical cytology image segmentation challenges in ISBI 2014 and ISBI 2015. The experimental results demonstrate superior performance of the proposed MPFW in terms of segmentation accuracy, detection rate, and time complexity, compared to recent peer methods.

***Keywords*—Overlapping cell segmentation, cervix cytology, shape marker, distance map, watershed segmentation, Chan-Vese active contour.**

I. Introduction

CERVICAL cancer, a malignant tumor in the tissues of the cervix, is one of the most serious threats to women health worldwide. According to World Health Organization [1], this cancer is responsible for more than 270 thousand deaths every year, and about 85% of these death cases occur in the developing countries owing to lack of access to screening and treatment services. Notwithstanding these facts, cervical cancer is one of those rare cancer groups which can be cured if detected at an early stage by Pap smear test, where a sample of cervical cells is deposited onto a glass slide for microscopic examination. In the last three decades, Pap test has dramatically reduced the incidence and mortality rates of cervical cancer in developed countries with an effective screening program [2], [3]. However, Pap test is still a manual screening task performed by pathologists, who should be skilled enough to localize the abnormal cells among thousands of cells. This manual procedure is not only difficult and time-consuming, but also results in inaccurate diagnoses owing to intra- and inter-observer variability. To this end, a machine-assisted screening and diagnosing system will bring significant benefits to combat cervical cancer, and accurate segmentation of cell nuclei and cytoplasm in the digitized Pap smear images is the essential first step.

Despite the recent development in analyzing Pap smears, establishing an accurate and completely automatic segmentation for both nuclei and cytoplasm of cervical cells in the digitized Pap images remains an open problem. Fig. 1 (a)-(d) show the procedures of generating the digitized Pap images, like those used in this study. A cervical cytology slide is examined under a microscope (a), to capture different fields of view (FOVs), each with a 3D stack of images acquired at multiple focal planes (b), where some of the cells are out of focus (c). The *3D* stack is then processed to generate a single extended depth-of-field (EDF) image where the entire field of view is supposed to be perfectly in focus [4], as shown in Fig. 1 (d). Unfortunately, the generated Pap images usually have a complex structure, resulting from the inconsistent staining, the noisy background, the poor contrast of the cell cytoplasm, the overlap among cervical cells, and the presence of mucus, blood, and artifacts, as shown in Fig. 1 (e). It is thus challenging to automatically achieve accurate segmentation of cervical cells in Pap smear images, where cellular components often cannot be reliably attributed to individual cells.

In this study, we establish an accurate Multi-Pass Fast Watershed (MPFW) method to automatically segment each cell's nucleus and cytoplasm from overlapping clusters in synthetic, real EDF, and multi-layer Pap images. The proposed methodology differs from other segmentation methods for overlapping cervical cells in the literature [5]–[18], in two key points: (1) it is designed to be an adaptable and cost-effective method with highly efficient algorithmic components; (2) it works with not only the EDF images, but also the FOV images. In addition, the proposed methodology demonstrates superior performance in both nuclei and cytoplasm segmentation compared to existing successful methods. This has been achieved by three watershed passes in our MPFW. The first watershed pass incorporates intensity gradient information into the watershed framework to

*A. Tareef, Y. Song, D. Feng, and W. Cai are with the Biomedical and Multimedia Information Technology (BMIT) Research Group, School of Information Technologies, University of Sydney, NSW 2006, Australia (email: atar8654@uni.sydney.edu.au).

H. Huang is with the Department of Electrical and Computer Engineering, University of Pittsburgh, USA.

M. Chen is with the Electrical and Computer Engineering Department, University of Albany State University of New York, USA, and with Robotics Institute, Carnegie Mellon University, USA.

Y. Wang is with the Department of Electrical and Computer Engineering, Virginia Polytechnic Institute and State University, USA.

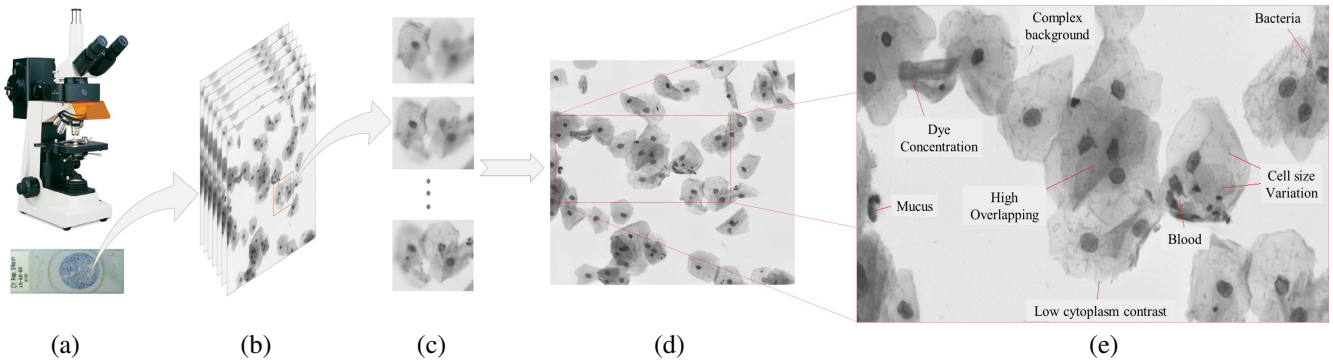

Fig. 1. (a) shows the Pap image acquisition from a cervical cytology slide tested under a microscope. (b) shows a *3D* stack of focal plane images acquired from the slide, where different cells are in and out of focus (c), which is then converted into a single EDF microscope image (d). Image (e) expounds the challenges of overlapping cervical cell segmentation owing to the poor cytoplasm contrast, complex background, existence of blood, mucus, bacteria, dye concentration, and high degree of overlap among cells. All these factors impact the desired segmentation.

segment the cell nuclei, whereas the cytoplasm segmentation, which is the main contribution of this study, is achieved by two watershed passes. Specifically, the second watershed pass is based on two markers within the same cell region that indicate the cell shape and location information, to segment isolated and partially overlapped cells. The third pass introduces a mutual iterative watershed that is independently conducted for each nucleus in the largely overlapping cells not segmented in the previous pass. Elliptical modelling is also performed to deform the line-shape watershed contour to give a more realistic cell segmentation. The proposed MPFW is evaluated and compared to the state-of-the-art methods proposed in the past five years on several datasets of synthetic, real EDF, and multi-layer Pap images, with competitive results in both nuclei and cytoplasm segmentation accuracy, as well as method adaptability and compute complexity.

The manuscript is organized as follows. Section II gives a brief survey of the current segmentation methods for Pap images. Section III describes our proposed methodology. Section IV describes the material and experimental setting. The experimental results and discussion are presented in Section V. Finally, the conclusion is provided in Section VI.

II. Literature Review

Existing methods for cervical cell segmentation can be classified into four diverse groups: 1) studies for segmentation of cell nuclei, 2) studies for segmentation of cellular components (i.e., nuclei, cell mass, and background), 3) studies for segmentation of the single cells without any overlap, and only recently 4) studies to extract both nuclei and cytoplasm from a cell mass of touching or overlapping cells. We provide brief review of these different groups of methods in this section.

A. Segmentation of Cell Nuclei

Methods for single and overlapping nuclei segmentation have been extensively studied over the years. In an early attempt, Bamford et al. [19] introduced a method to extract the cell nuclei from cervical cytology images using Viterbi search-based dual active contour algorithm, which is proved to be more efficient than the conventional active contour algorithm. Several methods have then been proposed based on morphological analysis [20], [21], watershed transform [22], [23], unsupervised classification [24], and deformable models [25]–[28] to delineate the boundaries of single and overlapping cervical nuclei. For instance, Plissiti et al. [29] proposed a segmentation method for overlapping cell nuclei based on morphological operations and active contour model. A watershed-based method was presented in [23], where a morphological reconstruction is employed to extract the nucleus markers, which are then used with watershed transform to identify the nuclei boundaries. Then, the false nuclei candidates are eliminated based the fuzzy C-means clustering algorithm. Chen et al. [30] introduced a supervised learning-based template matching method to segment touching nuclei from microscopy images. This method used training nuclei samples for building a statistical model capturing the texture and shape variations of the nuclei structures to be used for segmentation. In [31], a new segmentation method for nuclei of overlapping cells is introduced based on a circular shape function (CSF) and fuzzy c-means clustering.

In general, the existing studies on the segmentation of cervical cell nuclei have achieved a satisfied performance. The accurate nuclei segmentation is a prerequisite for successful segmentation of individual cell cytoplasm, which is quite important for subsequent cellular analysis.

B. Segmentation of Cellular Components

The goal of the second group of studies, beside segmenting the single/ overlapping nuclei, is to separate the whole cell masses from the background. An example of such methods can be found in [32], [33]. In [32], a non-parametric hierarchical segmentation algorithm is performed to initially segment the Pap image, and then, support vector machine is used to classify the obtained segments based on their spectral, shape and gradient features. In [33], Gencctav et al. introduced a method employing automatic thresholding to separate the cell masses from the background, and then, multi-scale hierarchical watershed and a binary classifier are applied to separate the nuclei from cell masses. Yet, these methods delineate the

boundary of the whole cell mass, instead of delineating the boundary of each individual cell cytoplasm.

C. Segmentation of Isolated cell

Single cell segmentation from Pap image has been approached in several works. Edge enhancement [34], unsupervised classification [35], and deformable models [36]–[38] are common choices for segmentation of single or isolated cells. For instance, Lin et al. [34] proposed a segmentation method based on a series of edge enhancement techniques. The gradient vector flow (GVF) is also adapted to extract the nuclei and cytoplasm boundaries of individual cells in Pap images in [38]. This method estimates the orientation of the GVFs in the pixels near to an edge. Li et al. [36] also applied the GVF in a radiating fashion over the GVF field. In [35], a patch-based fuzzy C-mean clustering and morphological reconstruction are conducted to segment the isolated cells. Although most of these methods produce good segmentation results for both nuclei and cytoplasm, they cannot process the touching and overlapping cells, which are typically present in cytology specimen.

D. Segmentation of Overlapping Cell

The segmentation of nuclei and cytoplasm pairs of cervical cells with overlap is a crucial task in automated cervical cancer screening, since the similarities between the overlapping and malignant cells may result in misclassification of the overlapped regions [39], [40]. The earliest studies for overlapping cell segmentation attempt to segment the nucleus and cytoplasm of touching or partially overlapping cells. For instance, Béliz-Osorio et al. [41] utilized a locally constrained watershed transform to segment touching cells. Another segmentation method for touching nuclei and cytoplasm is introduced in [42] based on a graph-partitioning via superpixel and multi-scale convolutional network (MSCN). In [43], the cytoplasm is segmented with a global multi-way graph cut, whereas the nuclei were segmented using an adaptive and local graph cut, which allows the combination of intensity, texture, boundary and region information. The touching regions are then splitting by integrating two concave points-based approaches. Another method for touching cell segmentation is proposed in [44] based on morphological filtering and curvelet initialized level set evolution.

For partially overlapping cells, the segmentation method in [7] applies gradient thresholding to extract the cell boundaries, followed by a set of morphological operations to infer the cytoplasm segmentation. In [10], morphological reconstruction and thresholding are utilized to detect the cell nuclei, whereas the individual cytoplasm of partially overlapping cells are delineated through a hierarchical deformation process.

Due to the importance of this issue, two grand challenges on the segmentation of overlapping cervical cells from synthetic, EDF, and multiple focal-plane images, have been recently held in conjunction with the IEEE International Symposium on Biomedical Imaging (ISBI) in 2014 and 2015. On the provided datasets by these challenges, a limited number of methods have been suggested to address the problem of overlapping cell segmentation, and they achieved satisfying performances [5], [6], [8], [9], [11]–[18], [45]. This section reviews these methods presented in the literature for the above segmentation challenges.

Numerous segmentation methods with satisfying performances have been proposed using the first dataset consisting of *2D* synthetic and real EDF images. For instance, Ushizima et al. [5] introduces a method based on superpixel partitioning and Voronoi diagram. Several methods have also been designed to optimize the segmentation performance by incorporating level set evolution with shape prior, such as elliptical shape prior [6], [45], star shape prior [9], geodesic-based shape prior [8], and dynamically-learned shape prior [11], [18]. Another segmentation method is proposed in [17] based on sparse shape deformation guided toward the target cell shape using representative features that are captured from a well-established initial shape.

In addition, segmentation of overlapping cells from a *3D* stack of images acquired at multiple focal-planes has the potential to produce more exquisite segmentation, even though, it is fairly complicated because of the fuzzy cell contours for the out-of-focus cells in the images. Various methods have been proposed to delineate the overlapping cell borders using multiple focal-plane images given by the second ISBI challenge. In [13], the cell cytoplasm is segmented by dividing the focal-plane images into grid squares and classifying them based on gradient features. An improved version of this method is then introduced in [14] to approximate the cell boundaries by a new distance metric and gradient-based refinement process. Ramalho et al. [12] enhanced the segmentation method in [5] to work with multi-layer volumes. The cytoplasm segmentation is performed by combining the cell contours extracted by Laplacian of Gaussian (LoG) method from multi-focal images with the corresponding contours extracted by Canny detector from EDF image. Lee et al. [15] designed a segmentation method to extract accurate cell boundaries by labelling image superpixels into the cells with the nearest nucleus, and refining the contour by cell-wise graph cuts.

In spite of the satisfying performance given by the above methods on the two datasets, most of them have adopted complex techniques and require extensive parameter tuning, hence cannot be easily adapted to a new dataset of cell images. Furthermore, most of these methods are computationally expensive. Since these methods are supposed to be employed in a typical laboratory with modest computing facilities, the applicability of the segmentation systems must become an important consideration.

III. The Proposed Methodology

The proposed methodology is performed in three passes of watershed transform intelligently controlled by representative marker identification functions, including (A) the first-pass watershed for nuclei localization, (B) the second-pass watershed for touching and overlapping cytoplasm segmentation, and (C) the third-pass watershed for largely overlapping cytoplasm segmentation in an iterative fashion.

In general, marker-controlled watershed transform has been widely used for image segmentation because of its advantages

of simplicity, rapidity, flexibility and absence of adjustable parameters [46]. The proper marker definition is the key to successful use of the marker-controlled watershed, as those markers with proper marking function, determine the final segmentation performance [47]. Therefore, MPFW incorporates a representative and properly-identified set of markers with each of the following watershed passes.

A. First-pass Watershed for Nuclei Localization

Our first-pass watershed phase entails region partitioning to reduce computational cost and enforce local consistency, followed by contour-based watershed transform to localize the nuclei within the cell mass. This phase starts by separating the image foreground (i.e., cell mass or clump) from the background, by employing Triangle algorithm [48] on the median filtered Pap image. The triangle algorithm separates the image into two classes by establishing a line between the peak of the image histogram and its farthest end, and thereafter, the appropriate threshold is identified as the point with the maximum distance between the histogram and the established line. Consequentially, tiny background objects unlikely to be cell masses are eliminated.

Then, mean-based partitioning is introduced to generate a rough image with an obvious difference between nuclei and other cellular components. While image partitioning with mean shift algorithm offers homogeneous regions for each intensity sub-range, these regions are asymmetrical in shape or size. This may lead to divide some symmetrically-shaped objects into multiple partitions or include them with other partitions. Providing that the nuclei in pap images usually have symmetric shape, i.e., ellipse, we propose to develop our mean-based partitioning technique to generate a rough version of the image.

First, regularized superpixel partitioning is performed to fragment the image into regular partitions, then, the mean of each partition is computed and replaced all pixels in the partition. SLIC algorithm [49] is chosen here as it considerably reduces the computational cost and could get a high accuracy of up to 95%. SLIC algorithm uses two factors; one determines the number of pixels in each partition, and the other one tells how much it should care about distance and color versus distance and geographical distance and location. These two factors are assigned to 25 and 0.01, respectively, for five different datasets used in this study, as described later in Section IV. This process generates an intermediate image, where many irrelevant details in the noisy Pap image are filtered and the edges between the different cellular components are highlighted, with the cluster shape taken into consideration during partitioning.

The next step extracts the high-gradient pixels representing the object contours to use them directly as a barrier to the water flow in the watershed transform. Specifically, the Sobel gradient of the generated intermediate image is obtained, and then, automatic Otsu's thresholding is applied to extract the high-gradient contour pixels. Next, morphological closing with a disc structuring element of diameter 1 is employed to link the adjacent pixels and build connected contours, which are used as the markers of watershed transform. Marker-controlled watershed is then applied, and the resultant watershed regions with closed contours are most probably nuclei regions. There will be some small closed regions resulted from blood or mucus that generate closed boundaries. Some overlapping cells with clear boundaries may also get closed contours as well. Such regions are basically marked as nuclei candidates, but they can be filtered out based on their shape and size properties. Finally, morphological dilation and holes-filling operators are applied to build a solid nuclei mask, followed by Chan-Vese level-set with only two iterations to connect a single nucleus that is divided into multiple parts in the region partitioning step.

Algorithm 1 The overlapping cell segmentation processes.

procedure INDIVIDUAL CYTOPLASM SEGMENTATION
Input: Nuclei image I_{Nu}, Background image I_{BK}
Output: Individual cell C

% SECOND-PASS WATERSHED
  $D_{in} \leftarrow H_t(-D_E(I_{BK}), h)$ % Inner distance function
  $D_{out} \leftarrow H_t(D_E(I_{Nu}), h)$ % Outer distance function
  $M_C \leftarrow H_t((2 \times D_{in} + D_{out}), h)$ % Integrated marking function
  $M_G \leftarrow H_t(D_G(\sim I_{BK}, I_{Nu}), h)$ % Geodesic marking function
  $S_C \leftarrow W(M_C)$, $S_G \leftarrow W(M_G)$ % Watershed transform

  for C_c=1 To # regions in S_C **do**
    if # nuclei in C_c==1 **then**
      $C_g = S_G(Nu)$ % Corresponding geodesic cell
      ${C_c}^e = E(C_c, \Omega)$, ${C_g}^e = E(C_g, \Omega)$ % Ellipse modelling
      $C_f = {C_c}^e \vee {C_g}^e$ % Cells combination
      $C_f = C_f \wedge \sim I_{BK}$ % Contour adjustment
    else

% THIRD-PASS WATERSHED
      for i=1 To # nuclei Nu in C_c **do**
        ${Nu_i}^e = E(Nu_i, \Omega^d)$ % Enlarged nucleus-in-focus
        $I'_{Nu} = I_{Nu} \vee {Nu_i}^e$ % Temporary nuclei image
        $D'_{out} \leftarrow H_t(D_E(I'_{Nu}), h)$ % Intermed. marking function
        $S' \leftarrow W(D'_{out})$ % Intermediate watershed segmentation
        $C_m = S'(Nu_i)$, $C_g = S_G(Nu_i)$ % Corresponding cells
        ${C_m}^e = E(C_m, \Omega)$, ${C_g}^e = E(C_g, \Omega)$ % Ellip. modelling
        $C_f = {C_g}^e \vee {C_m}^e$ % Cells combination
        $C_f = C_f \wedge \sim I_{BK}$ % Contour adjustment
      end
    end
  $C = \mathcal{E}(C_f)$ % *Chan-Vese* modelling
  $C = C \wedge \sim I_{BK}$ % Contour adjustment to remove false pixels
  Eliminating the small candidates based on a present threshold Γ

end procedure

B. Second-pass Watershed for Cell Segmentation

The cytoplasm segmentation is achieved by the second and third MPFW passes, and it is the main contribution of this study. Algorithm 1 summarizes the overlapping cell segmentation processes performed by watershed segmentation intertwined with elliptical modelling and contour refinement.

The second and most crucial pass in our MPFW is designed to segment most of cells in the image based on the localized nuclei and cell mass, as shown in Fig. 2. For this purpose, this pass incorporates the advantages of different distance transforms based on two sets of markers to effectively represent the

individual cell cytoplasm. Particularly, two marking functions, i.e., integrated inner-outer Euclidean distance transform (EDT) and geodesic distance transform (GDT), are combined to overcome the over- and under-segmentation problems. Moreover, a set of nuclei markers characterizing the cell number and location, are incorporated with geometric-based marker characterizing the cell shape, for better segmentation of overlapping cells in Pap image.

Euclidean distance transform (EDT) is one of the most extensively used marking function [46], including inner and outer distance transforms. The inner distance map converts a binary image into a distance map where each pixel has a value corresponding to the minimum distance from outer markers, whereas the outer distance transform measures the minimum straight-line distance from given inner markers. Fig. 2 (b) and (d) show examples of the inner and outer DT that are computed based on the background image shown in Fig. 2 (a) and the nuclei image in Fig. 2 (b). The corresponding segmentation of the inner and outer DT by marker-controlled watershed is displayed in Fig. 2 (d) and (f), respectively. Moreover, Fig. 3 displays an example of a cell mass with missing and over-segmented nuclei, where (b)and (c) present the watershed segmentation using the inner and outer distance maps, respectively, for the output from the first watershed pass shown in (a).

The inner distance transform has the potential to preserve the physical characteristics and resemble the shape of the desired cells based on the provided markers, as shown in Fig. 2 (c). In addition, the inner distance map gives a good indication for the widely overlapping cells that cannot be accurately segmented with a single watershed transform. However, it suffers from some drawbacks (see Fig. 2 (d) and Fig. 3 (b)): 1) inaccurate watershed lines because of the reduction in the pixels elevation along the cutting lines between the overlapping cells when they move away from the cell mass boundary; 2) the over-segmentation for some elongated cells where two or more regional minima are appeared; 3) the under-segmentation for some overlapping cells, as it cannot guarantee that there will be a regional minimum corresponding to each cell in the overlapping cluster. This occurs when two or more cells are located closely in the same convex cluster, hence, their regional minima are connected with a valley.

On the other hand, while the outer distance transform based on nuclei guarantee one-to-one correspondence between the markers and cells, it also has several drawbacks (see the example in Fig. 3 (c)), including 1) the under-segmentation where some cells associated with missed nuclei in the first watershed pass will be missed even if those cells are single or slightly touching cells; 2) the over-segmentation caused by the false positive nuclei detection; 3) the high pixel-based false negative rate, where the nuclei-based watershed sometimes trims the cytoplasm border. Most of those cases could be handled if the outer distance map include shape information, which has been proven to be beneficial for watershed segmentation [50].

Another kind of marking functions used for cell segmentation is the geodesic distance transform (GDT) [51]. The geodesic distance is the length of the shortest path between the true pixel in a binary image and the nearest true pixel

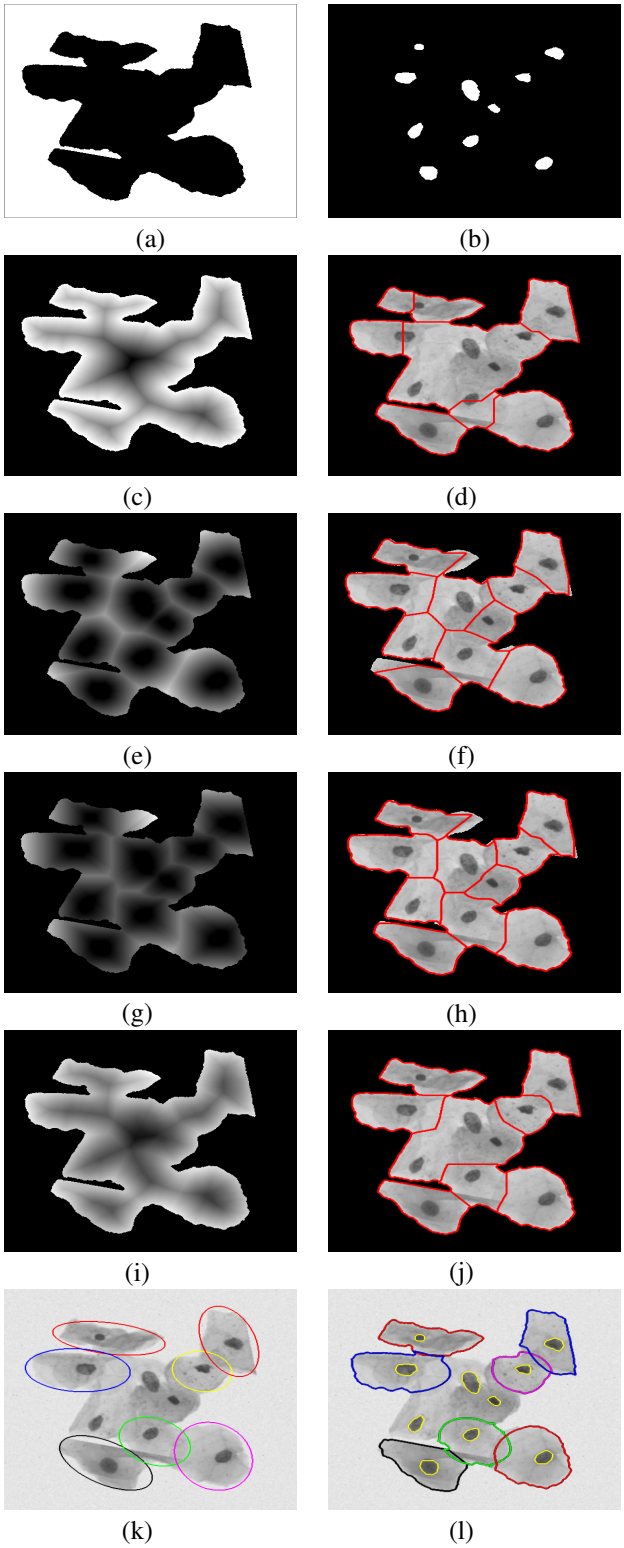

Fig. 2. Watershed segmentation using different marking functions based on (a) background and (b) nuclei markers, including (c) classical D_{in} on the background image with the corresponding segmentation in (d), (e) D_{out} for nuclei image with its segmentation in (f), (g) D_G for the nuclei and cell mass image with the corresponding segmentation in (h),(i) represents our integrated distance map with its segmentation in (j). (k) represents elliptical modelling process, and the corresponding results after contours adjustment in (l).

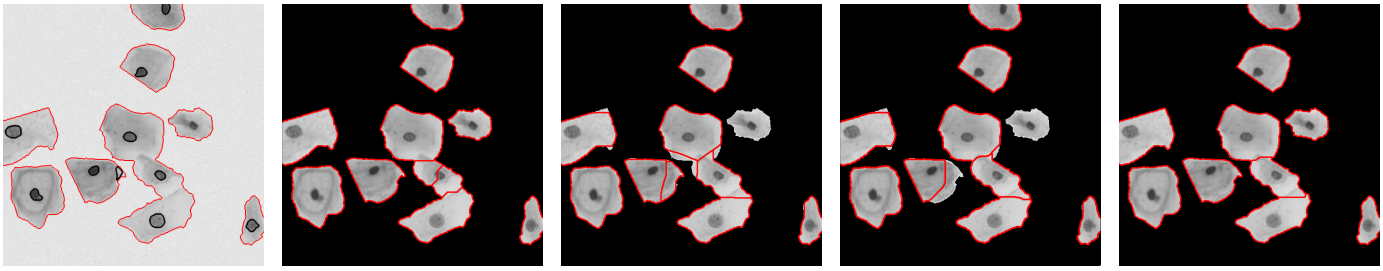

(a) (b) (c) (d) (e)

Fig. 3. The watershed segmentation based on the nuclei and background segmentation in (a) using the classical D_{in} on the background image (b), the D_{out} for nuclei image (c), the D_G for the nuclei and cell mass image (d), and our integrated distance map (e). As shown, D_{in}-based segmentation preserves the shape of most cells, but does not guarantee the one-to-one correspondence. In contrast, while segmentation with D_{out} and D_G guarantees the one-to-one correspondence, the cells of missed nuclei cannot be detected and the cell shape is not taken into consideration. All these drawbacks have been tackled with our integrated marking function, as shown in (e).

in a given mask. Examples of the GDT-based segmentation are displayed in Fig. 2 (h) and Fig. 3 (d). As shown, the GDT has the same advantages and disadvantages of the outer EDT, but with more true positive detection for the cytoplasm boundary pixels. Nevertheless, it still confronts the under- and over-segmentation problems.

In summary, the available marking functions have some advantages and disadvantages that cannot be ignored. In addition, none of the available functions can offer overlapping segmentation. This inspired us to introduce a smart marker definition process incorporating the useful information of each marking before conducting the watershed. The designed marking process also enables excluding the widely overlapping cells from segmentation to be segmented later in an iterative fashion (see Fig. 2 (j)). Specifically, two marking functions are utilized based on two sets of markers. The first marking function is a combination of inner and outer EDT of cell nuclei and image background, and the second marking function is the GDT of the cell mass based on the cell nuclei. The integrated marking function successes in handling the drawbacks of the classical marking functions, as shown in Fig. 3 (e).

To obtain the first marker, the inner distance map is generated by firstly computing the Euclidean distance map $D_E(x, y)$ for the binary background image $I_{BK}(x, y)$ displayed in Fig. 2 (a). The distance transform assigns a number representing the distance between each image pixel (x, y) and the nearest non-zero pixel $(x', y') \in I_{BK}$, as follows:

$$D_E(x, y) = \inf_{(x',y')\in I_{BK}} \sqrt{(x - x')^2 + (y - y')^2}. \quad (1)$$

After that, the inverse of the resulted distance map is computed, where the inner regions of cell mass appear as minima. The pixels not belonging to the cell mass are assigned to Infinity. The minimal value is then assigned to the region outside the cell mass to be segmented, i.e., background, to obtain an appropriate distance map $D_{in}(x, y)$.

Subsequently, H-minima transform $H_t(I, h)$ is applied to the inverse distance map with depth threshold h of 1, so that over- and under- segmentation caused by regional irregularities can be reduced. H-minima transformation is a contrast-oriented simplification method [52] that suppresses undesired minima whose depth is lower or equal to a given depth h of the relief function R_I, representing the morphological reconstruction of image I. The threshold h separates the lower values that could, in turn, lead to over-segmentation, from the higher values that result in under-segmentation. H-minima transform of image I can be defined as follows:

$$H_t(I, h) = R_I(I + h). \quad (2)$$

The outer distance map $D_{out}(x, y)$ is also computed for the binary nuclei image $I_{Nu}(x, y)$ displayed in Fig. 2 (b). Finally, the combined marking function $M_{C_h}(x, y)$ is built by integrating these two distance maps with higher weight to $D_{in}(x, y)$ to exclude widely overlapping cells, and then, filtering with H-minima transform to further exhibit the barrier between the adjacent minima:

$$M_{C_h}(x, y) = H_t(2 \times D_{in}(x, y) + D_{out}(x, y)), h). \quad (3)$$

The resulted integrated marking function M_{C_h} is displayed in Fig. 2 (i) with the corresponding segmentation in (j). This marking function successfully represents the cell cytoplasm in many cases. Nonetheless, it is possible to get a wide eccentric minimum in the combined distance map. Such case may lead to separate a single cell into two or more regions. To avoid a possible over-segmentation, the geodesic distance transform, described in [52], is computed. The GD map $D_G(x, y)$ is built with respect to the seed locations specified by nuclei mask and the binary image belonging to the foreground area, i.e., cell mass. In particular, GDT assigns a number for each pixel (x, y) in the foreground image $\sim I_{BK}$, portraying the minimum length L of the path $\mathcal{P} = \{p_1, p_2, ..., p_l\}$ joining that pixel and the nearest true pixel in nuclei image $(x', y') \in I_{Nu}$:

$$D_G = min\{L(\mathcal{P})|p_1 = (x, y), p_l = (x', y') \text{ and } \mathcal{P} \subseteq\sim I_{BK}\}. \quad (4)$$

Finally, the second marking function $M_{G_h}(x, y)$ is generated by applying H-minima transform on $D_G(x, y)$, as follows:

$$M_{G_h}(x, y) = H_t(D_G(I_{Nu}(x, y)), h). \quad (5)$$

Marker-controlled watershed W is then performed twice using the combined marking function $M_{C_h}(x, y)$ to get the segmentation S_C, and the geodesic marking function $M_{G_h}(x, y)$

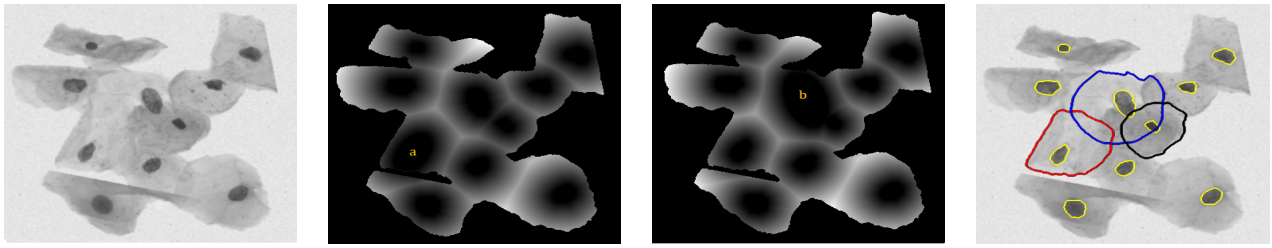

(a) (b) (c) (d)

Fig. 4. Intermediate results of the third-pass watershed; (a) the input image, (b) and (c) the distance maps for two iterations on nucleus a and b, (d) the final individual cell segmentation for the given watershed region.

to get the geodesic-based segmentation S_G. Thereafter, each obtained watershed region in the first segmentation $C_c \in S_C$ is classified into whether an individual cell (i.e., if there is a single nucleus inside) or cell cluster with multiple largely overlapping cells (i.e., if two or more nuclei are included within the watershed region). If the given C_c is identified as individual cell, then, C_c and the corresponding cell in the geodesic-based segmentation, $C_g \in S_G$, are ellipsoidal modelled $E(.,\Omega)$ in an image domain Ω by fitting ellipses algorithm [53], and adjusting the ellipse points located outside the cell mass (i.e., $\sim I_{BK}$) to the nearest mass border. By this way, the cell contours in the overlapping area are curved for more realistic cell contour than the straight lines imposed by watershed segmentation (see Fig. 2 (k)). Finally, the resulted modelled cells, i.e., ${C_c}^e$ and ${C_g}^e$, corresponding to the S_C and S_G watershed regions, respectively, are consolidated via inclusive OR operator $\vee$ to obtain the final segmentation of this stage $C_f = {C_c}^e \vee {C_g}^e$ (see Fig. 2 (l)).

In case where the S_C watershed region is classified as a cluster of largely overlapping cells, the third-pass watershed transform is run on this given segment to extract the individual cells. The process is repeated for each nucleus in the cluster until all cells corresponding to detected nuclei are segmented. The next section provides details of this process.

C. Third-pass Watershed for Largely Overlapping Cell Segmentation

The third watershed pass aims to extract the individual cytoplasm of clusters that are not segmented earlier due to the obscure geometric information of its cells (see Fig. 2 (l)). Given that each detected nucleus N_i, $\{i = 1, 2, ..., n\}$ represents a single cell in the given watershed region, a mutual preference-based watershed is designed, where watershed is repeated for each nucleus inside the given watershed region, and in each iteration, the nucleus-in-focus is given a preference for larger domain over its adjacent nuclei. In particular, a temporary nuclei image $I'_{N_i}(x,y), \forall N_i \in \{N_1, N_2, ..., N_n\}$ is built, in which the size of the nucleus-in-focus is doubled to expand the bassinet where the water flow will move. Fig. 4 displays a largely overlapping cluster that is separated through the third watershed pass. Fig. 4 (b) and (c) represent the distance maps for two independent watershed iterations, in which a single cell is taken a preference for a larger segmentation over the other joint cells in its turn, resulting in an overlapped segmentation shown in Fig. 4 (d).

As the shape of the markers can be regarded as the first shape estimation of the overlapping cells, we use the ellipse modelling to double the nuclei size with preserving the elliptical shape of the nuclei. Thereafter, the outer distance transform is performed to convert the binary nuclei map into a distance map where every pixel has a value corresponding to the minimum distance from the nuclei markers. Since the EDT measures the distance from the elliptical nuclei, the obtained distance map resembles the shape of the overlapping cells, which are assumed to be elliptical. H-minima transform is then applied to compound the image minima area. Finally, the watershed is separately performed for each nucleus, as following:

$$S'_{N_i} = W(D'_{N_i}(x,y)), \forall N_i \in \{N_1, N_2, ..., N_n\}. \quad (6)$$

where S'_{N_i} is the intermediate segmentation of the overlapping cluster with respect to the nucleus-in-focus Nu_i. Only the segmentation of the corresponding cell to Nu_i is extracted from S'_{N_i} and this process is repeated till getting the segmentation for all cells in the given overlapping watershed region. As this watershed pass is mutually independent for each nucleus within the given region, the segmented cells will be naturally overlapped. Next, elliptical modelling is performed on those obtained cells, to finally get more realistic segmentation, as shown in Fig. 4 (d).

In addition, since controlled watershed does not take the cell intensity information into account, the contour of the provided segmentation remains a plausible guess based on the location and shape of the cells. Therefore, we presume that utilizing intensity-based refinement step can further enhance the segmentation performance. The cell mass in the Pap image is first equalized with contrast-limited adaptive histogram equalization [54] with 0.01 threshold to enhance its contrast. Subsequently, the refinement process is performed with the region-based active contours proposed by Chan and Vese in [55] due to its fast, flexible, and accurate implementation. Although we believe that employing some improved level sets can effectively enhance the segmentation performance, we seek to adopt simple, fast, and efficient methods to maintain the applicability of the segmentation system. The Matlab graphics processing unit (GPU) implementation of Chan-Vese algorithm is employed for faster segmentation.

The Chan-Vese energy model tends to minimize the energy function $\mathcal{E}(c_1, c_2, R) = \mathcal{E}_s(R) + \mathcal{E}_e(R)$ with respect to the cell contour (R), where $\mathcal{E}_s$ is the force to shrink the cell contour (R), $\mathcal{E}_e$ is the force to expand it, c_1 represents the average pixels' intensity inside R, and c_2 represents the average intensity outside R. The two forces get balanced when the contour reaches the actual cell contour, whereabouts R reaches its equilibrium. Finally, the cell candidates whose area are less than a predefined threshold defining the acceptable cell size, i.e., 2000 pixels for our datasets.

IV. Materials and Experiments

A. Image Datasets

For performance evaluation, five test datasets provided in the first and second "ISBI Overlapping Cervical Cytology Image Segmentation Challenge" [56], [57] were used. All datasets contain a varying number of cells with different degrees of overlap, contrast, and texture. Table I summarizes the details of the test datasets used in our experiments.

The first challenge (ISBI-14) dataset consists of 945 synthetic cytology images, divided into 45 training images, and two sets of test images: ISBI-14 test-90 dataset of 90 images, and ISBI-14 test-810 dataset of 810 images. In this study, we also include the synthetic dataset provided by the ISBI challenge organizers in their baseline method [45], consisting of 18 cervical cytology images. All those synthetic images were 512 $\times$ 512 gray-scale images generated by overlapping a collection of isolated cells extracted from real Pap smear slides, and reconstructed by applying random linear brightness transform, and a random rigid transform (i.e., rotation, translation and scale), and finally located on the synthetic image using an alpha channel (sampling from 0:88 to 0:99). The number of overlapping cells in those images is ranged between 2 and 10 and the overlap coefficient between pairs of cells is in one of the following ranges: [0, 0.1], [0.1, 0.2], [0.2, 0.3], [0.3, 0.4], and [0.4, 0.5] [58]. The ISBI-14 dataset also contains 16 real EDF images, including 8 training images and 8 test images. All images were annotated with the ground truths of cell nuclei and cytoplasm.

The second challenge (ISBI-15) dataset consists of 17 samples from different cervical cytology specimens, with 8 samples for training and 9 for test. Each sample is a collection of multi-layer cell volume and the corresponding EDF image of 1024 $\times$ 1024 pixels. Each sample image contains 20-60 cells distributed on a set of clumps with a varying number of cells and different degrees of overlap. For each multi-layer volume, a stack of twenty layers was acquired from the same specimen at different focal planes, with a focal depth separation of approximately $1\mu m$. The test images were annotated with the cytoplasm ground truths. Among those datasets, the test images are used in our experiments.

B. Evaluation Metrics

Several evaluation metrics were used to assess the performance of our nuclei and cytoplasm segmentation methodology. Particularly, the performance of our cytoplasm segmentation was assessed using the same evaluation measures used in the ISBI challenge [56], including the pixel-level Dice coefficient (DC), true positive rate (TP_p), and false positive rate (FP_p) for a 'good'cell segmentation, and the object-level false negative rate (FN_o) for remaining cell segmentation. The segmentation is considered to be good if the obtained cell segmentation O_{Seg} overlaps with the ground truth O_{GT} with a DC higher than a specific threshold. DC was computed as $DC = 2\ \frac{|O_{GT} \wedge O_{Seg}|}{|O_{GT}|+|O_{Seg}|}$, where $|.|$ denotes the number of pixels in the object. In our experiments, the performance of the proposed MPFW method was evaluated over a range of good segmentation DC thresholds: $\{0.5, 0.6, 0.7, 0.8\}$ to validate the effectiveness of our cytoplasm segmentation, whereas a single DC threshold of 0.7 was used in the ISBI challenges, and in our performance comparison as well.

Furthermore, the performance of our nuclei segmentation was evaluated using the same criteria developed by Gençtav et al. [33] for true nuclei detection. Specifically, the object-level precision and recall of nuclei detection were first computed. Then, the pixel-level DC, precision and recall values were computed for the correct detections.

V. Results and Discussion

This section presents the evaluation results of the proposed methodology quantitatively and qualitatively in terms of segmentation accuracy and time complexity. Furthermore, the proposed methodology was compared with the existing state-of-the-art segmentation methods for overlapping cervical cells that were applied on the same datasets, including the winning methods in the first and second ISBI challenges [56], [57].

A. Quantitative Evaluation

The quantitative evaluation of our cytoplasm segmentation performance over a range of DC thresholds, i.e., $\{0.5, 0.6, 0.7, 0.8\}$, was conducted and the results were displayed in Table II. According to the table, the proposed MPFW method offered satisfactory cell segmentation performance in all metrics at different DC thresholds. Our cytoplasm segmentation showed a stable performance on the first baseline dataset where the lowest DC obtained for all cells in that dataset was 0.75. Moreover, a consistent increase in DC, TP_p, and object-level detection rate TP_o was shown on the other datasets, with on average DC of 0.85 and TP_p of 0.93 for all segmented cells with DC <0.5. The worst obtained DC and TP_p at DC threshold of 0.5 on the ISBI-14 datasets were 0.89 and 0.94, respectively, which were high values indicating a good segmentation. The FN_o obtained on the first and second datasets remained low even when only segmentations with $DC > 0.8$ were included in computing FN_o. This means that most of our segmented cells on those datasets had high DC values, which was up to 1 for some cells. The highest TP_p for all segmented cells was 0.997 on the ISBI-14 datasets and 0.981 on the ISBI-15 dataset, indicating that the segmentation was quite close to the ground truth. The proposed method had a significant rise in FN_o on the real EDF and multi-layer datasets when DC threshold changed from 0.7 to 0.8, i.e.,

TABLE I. DESCRIPTION OF THE TEST IMAGE DATASETS USED IN OUR EXPERIMENTS.

Dataset	Source	Image type	Image size	# cells/ image	# images
ISBI-14 Baseline DS	ISBI organizers [45]	Synthetic	512 × 512	2-5 cells	18 images
ISBI-14 test-90 DS	First challenge [56]	Synthetic	512 × 512	2-10 cells	90 images
ISBI-14 test-810 DS	First challenge [56]	Synthetic	512 × 512	2-10 cells	810 images
ISBI-14 EDF DS	First challenge [56]	EDF	1024 × 1024	20-60 cells	8 test images
ISBI-15 test DS	Second challenge [57]	EDF & FOV	1024 × 1024	20-60 cells	9 samples 20 layers/each

TABLE II. OUR CYTOPLASM SEGMENTATION $((DC)/(TP_p)/(FP_p)/(FN_o))$ AT DIFFERENT DC THRESHOLDS FOR SYNTHETIC, EDF, AND MULTI-LAYER PAP IMAGE DATASETS.

	$DC >$**0.5**	$DC >$**0.6**	$DC >$**0.7**	$DC >$**0.8**
ISBI-14 Baseline DS	(.94)/(.95)/(.005)/(.00)	(.94)/(.95)/(.005)/(.00)	(.94)/(.95)/(.005)/(.00)	(.95)/(.96)/(.003)/(.06)
ISBI-14 test-90 DS	(.89)/(.94)/(.005)/(.06)	(.90)/(.95)/(.004)/(.08)	(.90)/(.95)/(.004)/(.11)	(.92)/(.95)/(.003)/(.20)
ISBI-14 test-810 DS	(.88)/(.94)/(.006)/(.09)	(.89)/(.94)/(.005)/(.12)	(.90)/(.95)/(.005)/(.16)	(.92)/(.96)/(.004)/(.27)
ISBI-14 EDF DS	(.86)/(.91)/(.002)/(.18)	(.87)/(.91)/(.002)/(.20)	(.88)/(.92)/(.002)/(.23)	(.91)/(.94)/(.001)/(.40)
ISBI-15 test DS	(.78)/(.93)/(.003)/(.18)	(.81)/(.93)/(.003)/(.26)	(.85)/(.94)/(.002)/(.34)	(.89)/(.97)/(.002)/(.59)

TABLE III. QUANTITATIVE CYTOPLASM SEGMENTATION RESULTS OF THE ISBI-14 SYNTHETIC DATASETS AS A FUNCTION OF THE NUMBER OF CELLS AND OVERLAPPING RATIO FOR GOOD SEGMENTATION WITH $DC > 0.7$.

	Overlapping ratio				
	$\in$ [0,0.1]	$\in$ [0.1,0.2]	$\in$ [0.2,0.3]	$\in$ [0.3,0.4]	$\in$ [0.4,0.5]
2 cells	DC=.97(.03),TP_p=.99(.02), FP_p=.00(.00),FN_o=.05(.22)	DC=.92(.07),TP_p=.98(.06), FP_p=.00(.00),FN_o=.03(.11)	DC=.92(.07),TP_p=.97(.06), FP_p=.00(.00),FN_o=.03(.11)	DC=.92(.06),TP_p=.97(.06), FP_p=.00(.01),FN_o=.10(.31)	DC=.91(.06),TP_p=.95(.06), FP_p=.00(.01),FN_o=.17(.34)
3 cells	DC=.97(.02),TP_p=1.0(.01), FP_p=.00(.00),FN_o=.02(.07)	DC=.90(.06),TP_p=.97(.04), FP_p=.01(.00),FN_o=.00(.00)	DC=.89(.07),TP_p=.95(.08), FP_p=.01(.00),FN_o=.15(.28)	DC=.88(.08),TP_p=.95(.06), FP_p=.01(.01),FN_o=.17(.28)	DC=.88(.06),TP_p=.90(.10), FP_p=.00(.00),FN_o=.33(.40)
4 cells	DC=.97(.04),TP_p=.99(.05), FP_p=.00(.00),FN_o=.00(.00)	DC=.91(.05),TP_p=.98(.05), FP_p=.00(.00),FN_o=.04(.09)	DC=.89(.07),TP_p=.95(.06), FP_p=.01(.01),FN_o=.19(.28)	DC=.89(.06),TP_p=.93(.07), FP_p=.00(.00),FN_o=.15(.22)	DC=.86(.07),TP_p=.90(.09), FP_p=.01(.00),FN_o=.38(.31)
5 cells	DC=.97(.04),TP_p=.99(.04), FP_p=.00(.00),FN_o=.03(.08)	DC=.90(.06),TP_p=.97(.05), FP_p=.01(.00),FN_o=.14(.20)	DC=.89(.06),TP_p=.96(.06), FP_p=.01(.00),FN_o=.30(.31)	DC=.86(.06),TP_p=.92(.08), FP_p=.01(.00),FN_o=.30(.35)	DC=.85(.07),TP_p=.89(.10), FP_p=.01(.00),FN_o=.23(.33)
6 cells	DC=.96(.05),TP_p=.98(.05), FP_p=.00(.00),FN_o=.02(.05)	DC=.89(.06),TP_p=.97(.05), FP_p=.01(.00),FN_o=.03(.07)	DC=.88(.07),TP_p=.95(.08), FP_p=.01(.00),FN_o=.13(.18)	DC=.86(.07),TP_p=.91(.08), FP_p=.01(.00),FN_o=.24(.24)	DC=.85(.07),TP_p=.89(.10), FP_p=.01(.00),FN_o=.39(.30
7 cells	DC=.96(.05),TP_p=.99(.05), FP_p=.00(.00),FN_o=.01(.03)	DC=.89(.06),TP_p=.97(.05), FP_p=.01(.00),FN_o=.06(.09)	DC=.88(.07),TP_p=.94(.07), FP_p=.01(.01),FN_o=.20(.26)	DC=.86(.06),TP_p=.90(.08), FP_p=.01(.00),FN_o=.27(.28)	DC=.86(.07),TP_p=.89(.11), FP_p=.01(.00),FN_o=.39(.32
8 cells	DC=.96(.04),TP_p=.99(.04), FP_p=.00(.00),FN_o=.03(.05)	DC=.89(.06),TP_p=.97(.05), FP_p=.01(.00),FN_o=.14(.16)	DC=.87(.07),TP_p=.93(.08), FP_p=.01(.00),FN_o=.13(.13)	DC=.86(.07),TP_p=.90(.09), FP_p=.01(.00),FN_o=.23(.29)	DC=.84(.07),TP_p=.87(.10), FP_p=.01(.00),FN_o=.33(.28)
9 cells	DC=.95(.05),TP_p=.98(.06), FP_p=.00(.00),FN_o=.01(.02)	DC=.88(.06),TP_p=.96(.05), FP_p=.01(.00),FN_o=.11(.17)	DC=.87(.07),TP_p=.93(.08), FP_p=.01(.00),FN_o=.15(.17)	DC=.86(.06),TP_p=.90(.09), FP_p=.01(.00),FN_o=.32(.27)	DC=.83(.07),TP_p=.87(.09), FP_p=.01(.01),FN_o=.36(.18)
10 cells	DC=.96(.05),TP_p=.99(.02), FP_p=.00(.00),FN_o=.00(.00)	DC=.89(.06),TP_p=.94(.08), FP_p=.01(.00),FN_o=.06(.09)	DC=.87(.06),TP_p=.93(.09), FP_p=.00(.00),FN_o=.06(.05)	DC=.85(.08),TP_p=.89(.09), FP_p=.01(.00),FN_o=.40(.31)	DC=.84(.08),TP_p=.87(.10), FP_p=.01(.00),FN_o=.24(.11)
Average	DC=.96(.04),TP_p=.99(.05), FP_p=.00(.00),FN_o=.01(.02)	DC=.89(.06),TP_p=.97(.05), FP_p=.01(.00),FN_o=.06(.04)	DC=.88(.07),TP_p=.94(.08), FP_p=.01(.00),FN_o=.14(.06)	DC=.87(.07),TP_p=.91(.08), FP_p=.01(.00),FN_o=.25(.10)	DC=.85(.07),TP_p=.89(.10), FP_p=.01(.00),FN_o=.31(.08)

from only 0.23 to 0.40 for the EDF dataset, and from 0.34 to 0.59 on the multi-layer dataset. This indicated that there were many cells on those datasets had DC values between 0.7 and 0.8, which were still good results according to the ISBI challenge guidelines.

The second evaluation, shown in Table III, assesses the performance of our MPFW with respect to varying number of cells and pairwise overlap coefficients, for a good segmentation threshold of $DC > 0.7$. These results were obtained with the ISBI-14 synthetic datasets, of which the cell number and overlapping ratio per image were provided with the datasets. According to the shown results, the performance of the proposed MPFW was semi-ideal with very high TP_p of 0.99 and low FP_p of zero for almost all images with overlap ratio $\in$[0, 0.1], regardless the number of cells. Our performance was also promising with high DC in the range [0.87, 0.92] for images with $\leq$0.2 overlap ratio. Likewise, the proposed MPFW was shown to be efficient in segmenting clusters of highly overlapping cells with up to 0.4 overlap between pairs of cells, provided that the number of cells within the cluster is four or less. When the overlapping ratio is relatively high, i.e., $\in$ [0.4, 0.5], MPFW had a slight degradation in the DC, TP_p, and FN_o as the number of cells was increased. Although that the segmentation of such case represents the main factor for performance degradation in cell segmentation methods, the proposed MPFW successfully segmented most of those highly overlapping cells with an average DC of 0.85 ($\pm$0.07) and TP_p of 0.89 ($\pm$0.10). Those results prove that our MPFW methodology is capable of producing robust segmentation even on challenging images with large clusters of highly overlapping cells.

Furthermore, our performance in terms of DC, FN_o, and TP_p for synthetic datasets was represented as a function of cell number and overlapping ratios in Fig. 5 (a), (b), and (c), respectively. As observed from the figure, the proposed method yielded a competitive DC for all images of less than three cells or $\leq$0.2 overlap between the cells. Yet, our segmentation was shown to be good with images with four to six cells,

provided that the overlapping ratio is $\leq$0.3. Our method had the worst DC when the overlapping ratio became more than 0.4 and number of cells exceeds eight cells per image. Fig. 5 (b) shows that our performance in FN_o is more sensitive to the changes in the overlapping degree than the changes in the number of cells. The proposed method successfully segments most of overlapping clusters of up to ten cells with less than 0.3 overlap between cells. When the overlapping ratio is higher than 0.3 and the number of cells exceeds eight cells, the false negative occurrences by MPFW was significantly augmented. As proven by Fig. 5, the degree of overlap has a great influence on all measures. This was because it became difficult to obtain the shape information from a highly overlapping cluster due to the appearance of valley connecting the regional minima in the inner distance map. This, in effect, led to producing an ellipse-based estimation of the cell shape during the third watershed pass. Regarding TP_p, the proposed method showed a high TP_p for images with up to 0.3 overlap between pairs of cells regardless the number of cells, and up to 0.4 overlap with less than five cells per image. Similar to DC, our TP_p performance degraded when the overlapping ratio is relatively high between 0.4 and 0.5, and number of cells was eight or more.

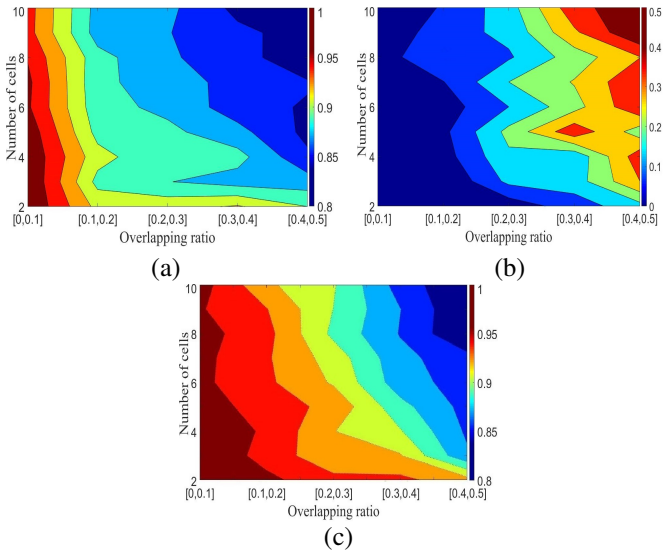

Fig. 5. Functional analysis of the proposed method in terms of (a) DC (in range [0.8 1]), (b) FN_o (in range [0 0.5]), and (c) TP_p (in range [0.8 1]). The diagrams show the evaluation metrics as a function of number of cells (y axis) and overlapping ratio (x axis).

In terms of nuclei segmentation, the proposed MPFW method yielded a high object-level $prec_o$ of 0.98 and rec_o of 0.96. Furthermore, the pixel-based results for our methodology consist of a $prec_p$ of 0.92($\pm$0.07), rec_p of 0.95($\pm$0.05) and DC of 0.93 ($\pm$0.04). These results demonstrate the effectiveness of the barrier-based watershed segmentation. The designed mean-based partitioning of the noisy Pap image successfully removes the irrelevant image details and highlight the difference between nuclei and other cellular components. This makes it easy to extract the nuclei boundaries with gradient thresholding process, which are then used to stop the water flow in the first watershed pass. With our nuclei segmentation process, most of the detected nuclei candidates are true cell nuclei, while the false negative cases occurred due to missing the nuclei shape or poor nuclei contrast. Therefore, we believe that some pre-processing operations to enhance nuclei contrast can be beneficial.

B. Qualitative Evaluation

The qualitative experiment consists of a visual inspection of the results of our cell mass separation, nuclei segmentation, and cytoplasm segmentation process. Fig. 6 shows some of our segmentation results using synthetic, real EDF, and multi-layer Pap images. As seen in Fig. 6 (b), the cell masses were accurately defined by triangle algorithm despite the complex background and poor contrast of the cell masses. Median filtering of the Pap image before separation helps to improve the clump segmentation performance. The proposed methodology also provided a precise estimation of the nuclei boundaries detected in the first watershed pass, as shown in Fig. 6 (c). Furthermore, Fig. 6 (d) proves that the boundaries of each individual cells in the overlapping regions were successfully detected by the proposed MPFW algorithm, showing promising segmentation of overlapping cells that is comparatively similar to the ground truth segmentation shown in Fig. 6 (e). Therefore, the proposed MPFW algorithm can be successfully used to separate the individual nuclei and cytoplasm from a clump of highly overlapping cells in different kind of datasets. There are some failure cases appeared in the EDF sample displayed in the third row of Fig. 6. This failure was mainly due to the lack of shape information from completely overlapping cells.

Overall, the proposed MPFW method provides a promising performance in terms of nuclei and cytoplasm segmentation thanks to the smart incorporation of cell shape and location information with watersheds in an iterative fashion. Our improved marker identification process successes in building accurate descriptors for cell shapes, as well as, helps to avoid over- and under-segmentation by establishing one-to-one correspondence between the cells and detected nuclei. In addition, the designed preference-based watershed can produce a fair cytoplasm segmentation for highly overlapping cells whose shape information are not available.

C. Comparison with Other Methods

The performance of our MPFW method was further quantitatively and qualitatively compared with the performance of the proposed methods in the past five years for automatic segmentation of overlapping cervical cells using the ISBI challenge datasets. First, we conduct a comparison between our segmentation results and the segmentation results of [10], [11], [18] using the test dataset provided by the ISBI-14 baseline method [45]. The proposed MPFW method was also employed on the ISBI-14 test-90 and test-810 synthetic datasets, and the obtained cytoplasm segmentation results were compared with the results of the presented methods in the literature on

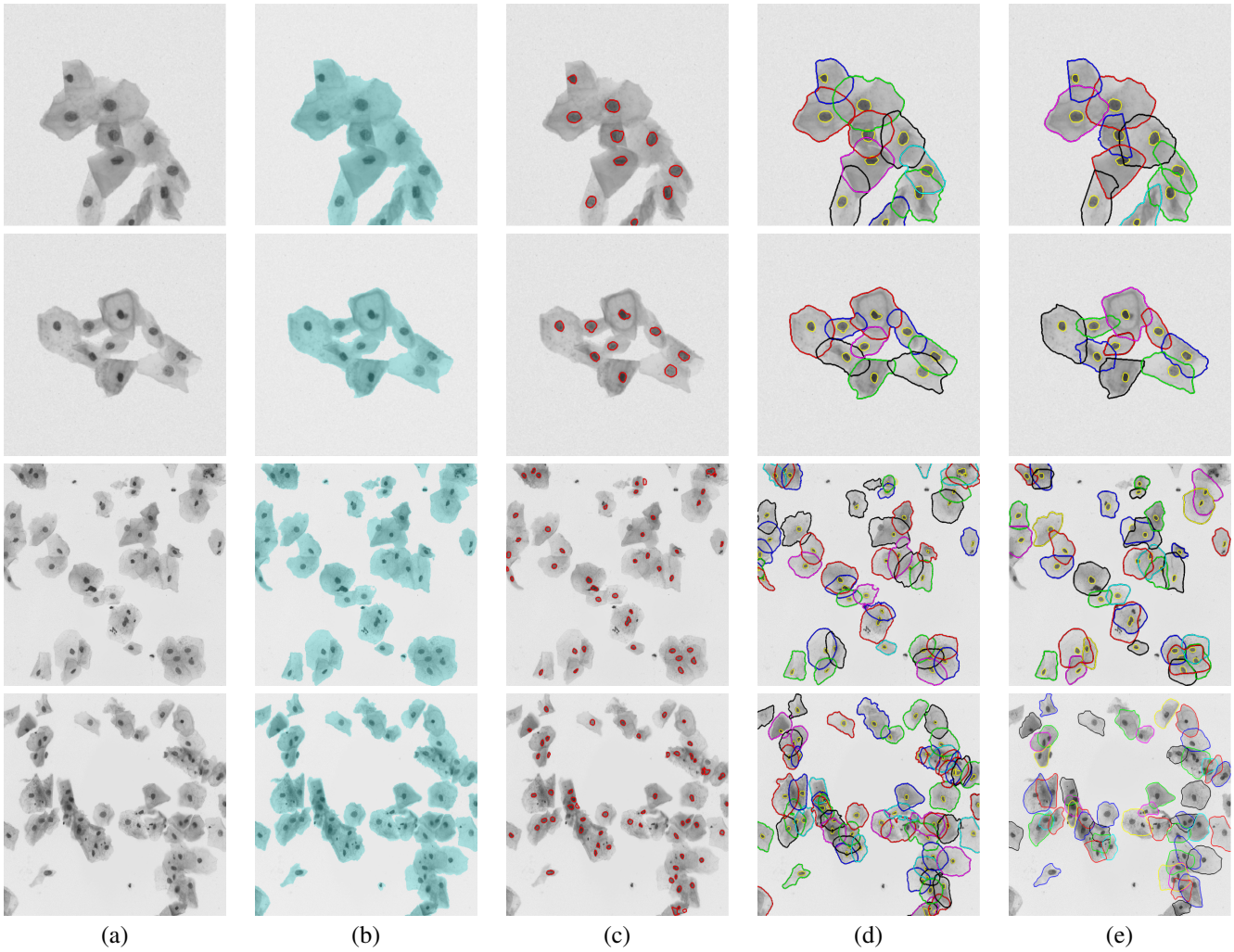

Fig. 6. Examples of our nucleus and cytoplasm segmentation results on synthetic (row 1 and 2), real EDF (row 3), and a single layer of multi-layer (row 4) Pap images; (a) the input Pap images, (b) the detected cell masses by Triangle algorithm, (c) the extracted nuclei in the first watershed pass, (d) the cytoplasm segmentation by the second and third watershed pass, and (e) corresponding ground truth images.

the same datasets, including the ISBI-14 challenge winners: Ushizima et al. [5], Nosrati et al [6] and their newly proposed method [9], the baseline method [8], and some later introduced methods [11], [15], [17], [18]. In addition, the performance of our cytoplasm segmentation on some real EDF Pap images was compared with the performance of the baseline method [8]. The proposed method was also applied to the ISBI-15 test dataset, and compared with the introduced methods on this dataset, including the challenge winners: Ramalho et al. [12], Phoulady et al. [13] and their newly proposed method [14], as well as, recently proposed methods presented in [15], [16]. For nuclei segmentation, only those methods reported their nuclei segmentation results, were included in the nuclei segmentation comparison. The comparison results are displayed in Table IV, Table V, and Fig. 7.

Table IV shows the comparison results of the cytoplasm segmentation performance, where bold numbers indicate superior results. The proposed MPFW showed a promising performance level in cytoplasm segmentation over all other methods. The designed cytoplasm segmentation achieved the best performance in terms of TP_p of higher than 0.94 for all datasets, and DC with an average of 0.91 for four datasets. Our MPFW can also be recognized with the high detection rate, which is demonstrated by the low FN_o of less than 16% for the synthetic datasets, and better detection rate than other state-of-the-art methods for the real EDF and multi-layer datasets.

In details, the obtained DC on the baseline dataset was 0.94 with up to 6% improvement over the other methods applied on the same dataset. Moreover, the obtained FN_O on the baseline dataset was zero, which indicates that MPFW successfully segmented all cells in this dataset. The proposed method also achieved the highest TP_p without increasing the FP_p. On the ISBI-14 test-90 dataset, the proposed MPFW obtained a superior performance in terms of DC, TP_p, and FN_o over the other six methods. Specifically, our obtained DC was 0.90 and TP_p was 0.95, with up to 4% and 12%

TABLE IV. COMPARISON RESULTS ($\mu \pm \sigma$) OF OUR CYTOPLASM SEGMENTATION AND THE STATE-OF-THE-ART METHODS.

Methods	FN_o	TP_p	FP_p	DC
Test dataset of [45]				
[45]	.21 ± .29	.92 ± .10	**.002 ± .005**	.88 ± .07
[10]	.07 ± .14	.94 ± .05	.005 ± .007	.92 ± .06
[11]	**.00 ± .00**	.93 ± .05	.005 ± .01	.91 ± .05
[18]	**.00 ± .00**	.92 ± .09	.004 ± .005	**.93 ± .06**
MPFW	**.00 ± .00**	**.95 ± .08**	.005 ± .007	**.93 ± .06**
ISBI-14 test-90 dataset				
[5]	.174 ± .210	.826 ± .130	**.001 ± .002**	.867 ± .083
[6]	.140 ± .170	.900 ± .090	.005 ± .004	.870 ± .080
[9]	.110 ± .170	.930 ± .090	.005 ± .004	.880 ± .080
[11]	.163 ± .223	.939 ± .064	.005 ± .005	.888 ± .076
[17]	.274 ± .277	.907 ± .088	.004 ± .005	.889 ± .073
[18]	.222 ± .240	.945 ± .071	.005 ± .005	.897 ± .077
MPFW	**.106 ± .167**	**.951 ± .072**	.004 ± .004	**.902 ± .074**
ISBI-14 test-810 dataset				
[5]	.267 ± .278	.841 ± .130	**.002 ± .002**	.872 ± .082
[6]	**.110 ± .166**	.875 ± .086	.004 ± .004	.871 ± .075
[8]	.315 ± .294	.905 ± .097	.003 ± .005	.893 ± .082
[15]	.137 ± .194	.882 ± .097	.002 ± .003	.897 ± .075
MPFW	.161 ± .249	**.946 ± .079**	.005 ± .004	**.898 ± .073**
Real EDF images [8]				
[8]	.36 ± .08	.90 ± .10	**.00 ± .00**	.87 ± .09
MPFW	**.23 ± .17**	**.92 ± .09**	**.00 ± .00**	**.88 ± .08**
ISBI-15 FOV test database				
[13]	.408 ± .163	.927 ± .098	.003 ± .002	.831 ± .079
[12]	.501 ± .180	.899 ± .113	.002 ± .001	.856 ± .078
[15]	.434 ± .168	.877 ± .123	**.001 ± .001**	**.879 ± .087**
[14]	.352 ± 000	.874 ± 000	**.001 ± 000**	.861 ± 000
[16]	.361 ± .158	.885 ± .101	.002 ± .001	.852 ± .076
MPFW	**.336 ± .130**	**.940 ± .080**	.002 ± .002	.851 ± .079

improvement, respectively, over the other methods on the same dataset. Furthermore, the highest detection rate was realized by our MPFW, i.e., 89% with up to 17% improvement over the other methods. Our FP_p was also less than the FP_p obtained by [6], [9], [11], [18].

Moreover, the proposed MPFW also achieved the best DC and TP_p on the ISBI-14 test-810 dataset, with up to 3% and 11% improvement, respectively, over the compared methods. The obtained FN_o was also much lower than the FN_o obtained by the ISBI-14 winning methods and baseline methods [5], [8]. Furthermore, the proposed MPFW had the highest performance in all measures with the real EDF images. Particularly, the obtained DC and TP_p were 0.88 and 0.92, compared with 0.87 and 0.90 obtained by the ISBI baseline method [8]. MPFW also provided 13% improvement in the detection rate over [8]. On the ISBI-15 dataset, the proposed methodology yielded remarkable results with very high TP_p and low FN_o compared to its counterparts. This indicates that our proposed method can effectively be used to segment individual cytoplasm of overlapping clusters from multi-layer cytology preparation volumes.

Although the cytoplasm segmentation process is the main contribution of this paper, our nuclei segmentation process has also shown a competitive performance. The object-level and pixel-level nuclei segmentation results of the proposed MPFW and the ISBI-14 segmentation methods [5], [6], [8] using the ISBI-14 synthetic test dataset are displayed in Table V. Compared to the challenge winning methods and baseline method, our proposed method had the best nuclei segmentation in four out of five measures. Most of the detected candidates by our method were true cell nuclei, proved by our high $prec_o$ of 0.98 and rec_o of 0.96, with up to 8% and 7% improvement over the ISBI methods. Also, our rec_p of 0.95 was higher than those obtained by the ISBI methods, with up to 8% improvement. The highest $prec_p$ of 0.97 was obtained by [5], however, this was at the expense of decreasing the rec_p based on the fact that the augment in the object size leads to include more true and false pixels in the segmentation. Those results indicated that our designed nuclei segmentation pass could be effectively used to extract the nuclei boundaries in Pap images. The designed mean-based partitioning step helps to minimize the within-class variance for the regions with high homogeneity, e.g., cell nuclei, and maximize the between-class variance. This, in turn, leads to more obvious boundaries that are used to control the first barrier-based watershed pass.

TABLE V. COMPARISON RESULTS OF OUR NUCLEI SEGMENTATION AND THE ISBI-14 CHALLENGE METHODS.

Methods	$prec_o$	rec_o	$prec_p$	rec_p	DC
[5]	.959	.895	**.968 ± .055**	.871 ± .069	.914 ± .039
[6]	.903	.893	.901 ± .097	.916 ± .093	.900 ± .053
[8]	.977	.883	.942 ± .078	.912 ± .081	.921 ± .049
MPFW	**.983**	**.959**	.906 ± .068	**.950 ± .051**	**.925 ± .041**

Furthermore, Fig. 7 displays a visual comparison between our nuclei and cytoplasm segmentation results and the segmentation results of ISBI-14 winning methods on synthetic and real EDF images provided in the challenge report [58]. As can be observed from the figure, the proposed MPFW algorithm is effective and reliable in delineating both nuclei and cytoplasm boundaries compared to its counterparts. MPFW provided better cytoplasm segmentation for the overlapping cells than the ISBI methods. For instance, the cell segmentation in [5] was done by straight lines splitting the cytoplasm between pairs of cells, which obviously is not realistic. This is usually the case with classical watershed segmentation. However, our proposed method copes with this by employing elliptical modelling and mutual iterated watershed. In addition, [5] showed several under-segmentation cases related to missing cell nuclei. Under- and over- segmentation was avoided in MPFW by incorporating two sets of markers, with robust marking functions, as well as improving the nuclei detection rate. In addition, the segmentation of [6] had a high pixel-level false negative rate, where the segmented cells are smaller than the actual cell segmentation, and delineated with a rough border that ignores the fine contour details. It is also seen that our method provided better pixel-level cell segmentation, with more regular cell contour, than the ISBI baseline method [8].

Overall, the quantitative and qualitative evaluation demonstrates the superiority of the proposed MPFW algorithm over the state-of-the-art methods for overlapping cell segmentation in Pap images. Besides being more accurate in terms of nuclei and cytoplasm segmentation, our method avoids the limitations in most of the existing segmentation methods, which can generally be outlined as being relatively complicated, compute-intensive, requiring extensive parameter tuning, and difficult to adapt to a new dataset of cytological cells. For instance, the level set-based segmentation methods, such as [6], [11], [18], [45], usually involve a handful of arbitrary parameters

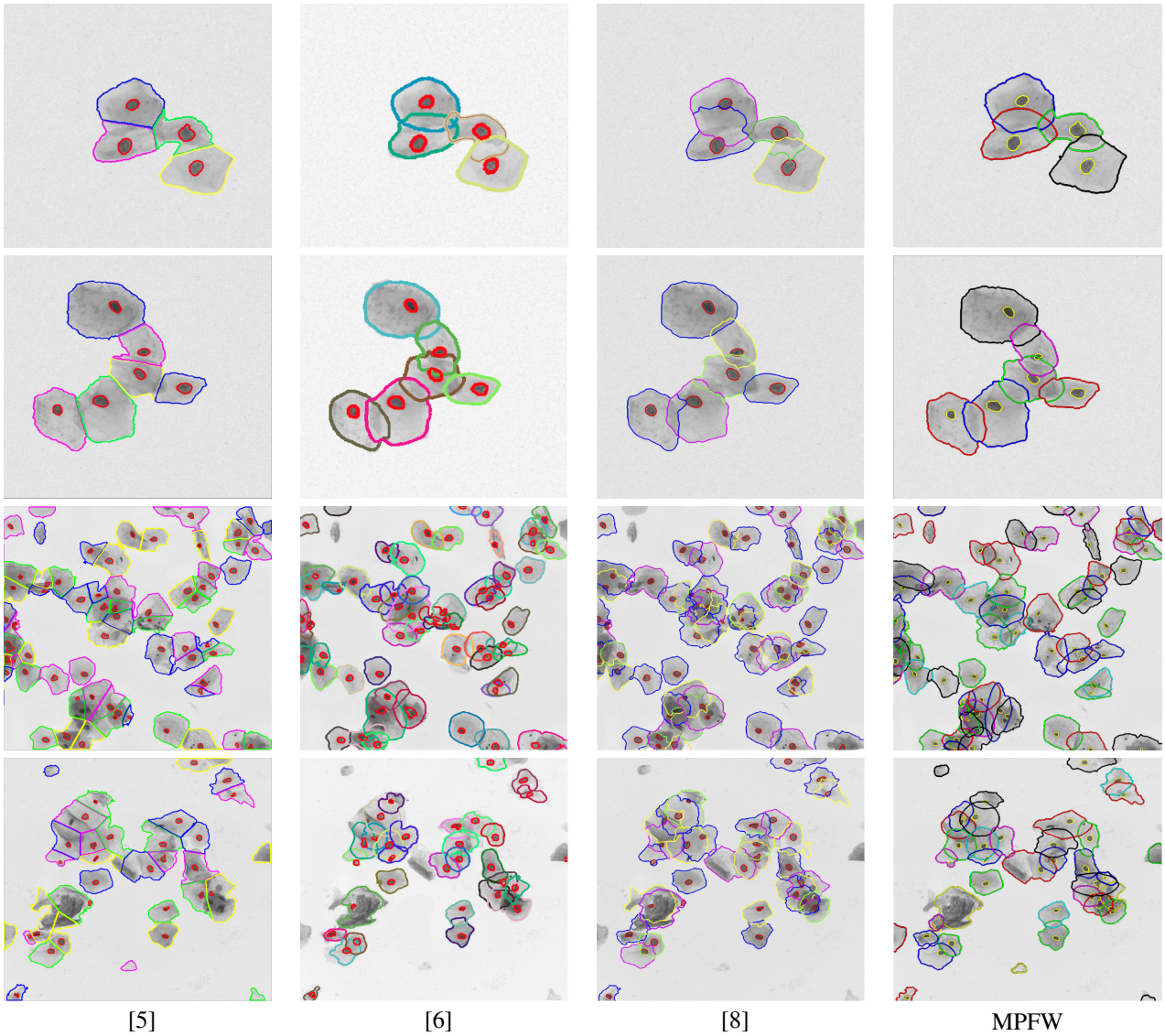

Fig. 7. Visual comparison between the proposed methodology and the ISBI-14 challenge methods using synthetic and real EDF Pap images, provided by [58].

empirically set for every dataset. This, in effect, reintroduces strenuous intervention of the users with no guarantee that the final chosen parameters are optimal. Another group of segmentation methods are based on shape deformation, such as [10], [17]. While shape-driven segmentation is one of the most reliable techniques to establish accurate cell analysis, still it is complicated and compute-intensive due to the costly training step and shape generation procedure. In addition, these methods may fail to segment some cells with infrequent cell shape in the training dataset.

With our MPFW method, the segmentation of each image is completely autonomous, where the incorporated shape information is independently built from each cell itself, not fixed shape prior [6], [9], [45], and not based on training shapes from a dictionary which usually has a large shape variations [10], [11], [17], [18]. This explains the superior performance of the proposed MPFW method with the five datasets over the current state-of-the-art methods. In addition, parameter adjustment is not necessary for our watershed cytoplasm segmentation to work with a new dataset, and only needed for the secondary refinement process of the segmented cells. This means that a fair performance for cytoplasm segmentation can be obtained regardless of the parameters chosen (from a reasonable range). There are three parameters used by Chan-Vese model employed for refinement; the smoothing and contraction-bias parameters that were set by default to 1 and -1, respectively, and the maximum number of iterations that was 30 iterations for the datasets used in this study. These values were initially chosen, and certainly, exquisite parameter selection offers better cytoplasm segmentation performance.

Although Chan-Vese refinement further enhanced our results, yet the watershed passes alone have the potential to

produce a promising cell segmentation with a DC of 0.899 ($\pm$0.08), TP_p of 0.895 ($\pm$0.10), FP_p of 0.002 ($\pm$0.004), and FN_o of 0.184 ($\pm$0.26) on the ISBI-14 synthetic datasets (e.g., see the segmentation results in Fig. 2 (l)). Furthermore, since our cytoplasm segmentation process does not depend on the cell intensity or texture information, it can be easily adapted to work with any new dataset.

D. Computational Complexity

The space and time-complexity of the segmentation method have become important, especially when dealing with large or high-resolution images, which is often the case in Pap smears images. Therefore, we aimed to design a robust segmentation method with low time-complexity and high-performance accuracy. Table VI displays the device specification and average computation time of the proposed MPFW method implemented with non-optimized Matlab code, compared with the computation time for other state-of-the-art methods on the ISBI-14 synthetic datasets. Ideally, we would like to carry all experiments on the same device, however, the implementation code of other methods are not publicly available yet. Although the implementation of Lu et al. method [8] is available, it needs a huge RAM, which is not the case with our device.

As shown in Table VI, the proposed method is proven to be cost-effective with an average of 5 seconds for nuclei and cytoplasm segmentation from 512 $\times$ 512 Pap images. This is less than a half of the time needed by the first ISBI-14 winning method, [5], which took 12 seconds per image. Moreover, MPFW is around 60 times faster than the baseline method [8] whose average computation time was $\sim$300 seconds. Our method is also faster than [9], and also provides better performance in nuclei and cytoplasm segmentation.

TABLE VI. COMPUTER SPECIFICATION AND COMPUTATIONAL TIME FOR THE PROPOSED AND STATE-OF-THE-ART METHODS.

Methods	Computer specification	Time/Image
[5]	12-core Intel, CPU 2.4GHz, 64GB RAM	12 sec.
[6]	PC, CPU 3.4 GHz,16 GB RAM	16.7 sec.
[9]	PC, CPU 3.4 GHz,16 GB RAM	6.6 sec.
[8]	PC, CPU 2.7 GHz, 8 GB RAM	$\sim$ 300 sec.
[11]	PC, CPU 3.2 GHz, 8 GB RAM	40.8 sec.
[17]	PC, CPU 3.2 GHz, 8 GB RAM	27.4 sec.
[18]	PC, CPU 3.2 GHz, 8 GB RAM	30 sec.
MPFW	PC, CPU 3.2 GHz, 8 GB RAM	**4.76 sec.**

In general, watershed transform is characterized by low computational cost and small number of parameters. We take advantage of those properties and design a multi-pass watershed intelligently controlled with cell shape and location information to dramatically reduce the computation time needed for cell segmentation compared to other methods in the literature. Despite the iterative performing of watershed in the third-watershed pass, this stage is only needed for widely overlapping cells, e.g., three out of ten cells with overlap ratio $\in$[0.4, 0.5] in the example shown in Fig. 4. The images with single, touching, and partially overlapping cells are segmented with the second-watershed pass.

Furthermore, the felicitous utilize of Chan-Vese model with few iterations, i.e., 30 iterations, on the graphics processing unit (GPU) further accelerates our methodology. The new computational improvements enable us to process large digital images faster and more effective.

VI. CONCLUSIONS

Despite the exciting development in the field of overlapping cell segmentation from cervical cytology images during the past five years, the focus of existing methods is mainly to achieve high performance in nuclei and cytoplasm segmentation on given datasets. In this paper, we have tried to widen our objectives to include the system applicability, speed, and straightforward implementation. For this purpose, we design MPFW; a simple and cost-effective segmentation method that is also capable of achieving superior segmentation performance than state-of-the-art methods.

The proposed methodology has been evaluated on several datasets of synthetic, EDF, and multi-focal Pap images. Compared to the existing segmentation methods for overlapping cervical cells, the proposed method exhibits the following merits: (1) it provides more accurate segmentation for both nuclei and cytoplasm; (2) it successfully segments most of overlapping cells with a low false negative rate; (3) it can work efficiently with both single and multi-layers Pap smear images; (4) it is simpler in implementation, and requires less time and space; and (5) the cell segmentation process is adaptable and can be natively extended to a new type of images without complicated experiments and extensive parameter tuning for individual datasets.

In the future, we intend to apply our method to other types of cell images. Our future work will also include designing a complete cell analysis system with a user-friendly interface for direct use by pathologists. The desired system will begin with generating an EDF image from given multi-layer cytology volumes, and end with classifying the cells into normal or abnormal cells and making a decision on the given sample.

REFERENCES

[1] W. H. Organization *et al.*, "WHO guidance note: comprehensive cervical cancer prevention and control: a healthier future for girls and women," 2013.

[2] E. Lăără, N. Day, and M. Hakama, "Trends in mortality from cervical cancer in the nordic countries: association with organised screening programmes," *The Lancet*, vol. 329, no. 8544, pp. 1247–1249, 1987.

[3] G. Johannesson, G. Geirsson, and N. Day, "The effect of mass screening in iceland, 1965–74, on the incidence and mortality of cervical carcinoma," *International journal of cancer*, vol. 21, no. 4, pp. 418–425, 1978.

[4] A. P. Bradley and P. C. Bamford, "A one-pass extended depth of field algorithm based on the over-complete discrete wavelet transform," in *IVCNZ*, 2004, pp. 279–284.

[5] D. Ushizima, A. Bianch, and C. Carneiro, "Segmentation of subcellular compartiments combining superpixel representation with voronoi diagrams," in *ISBI Overlapping Cervical Cytology Image Segmentation Challenge*. IEEE, 2014, pp. 1–2.

[6] M. Nosrati and G. Hamarneh, "A variational approach for overlapping cell segmentation," in *ISBI Overlapping Cervical Cytology Image Segmentation Challenge*. IEEE, 2014, pp. 1–2.

[7] A. Tareef, Y. Song, W. Cai, D. Feng, and M. Chen, "Automated three-stage nucleus and cytoplasm segmentation of overlapping cells," in *ICARCV*. IEEE, 2014, pp. 865–870.

[8] Z. Lu, G. Carneiro, and A. Bradley, "An improved joint optimization of multiple level set functions for the segmentation of overlapping cervical cells," *IEEE Trans. Image Process.*, 2015.

[9] M. Nosrati and G. Hamarneh, "Segmentation of overlapping cervical cells: A variational method with star-shape prior," in *ISBI*. IEEE, 2015, pp. 186–189.

[10] A. Tareef, Y. Song, M.-Z. Lee, D. D. Feng, M. Chen, and W. Cai, "Morphological filtering and hierarchical deformation for partially overlapping cell segmentation," in *DICTA*. IEEE, 2015, pp. 1–7.

[11] A. Tareef, Y. Song, W. Cai, H. Huang, Y. Wang, D. Feng, and M. Chen, "Learning shape-driven segmentation based on neural network and sparse reconstruction toward automated cell analysis of cervical smears," in *ICONIP*. Springer, 2015, pp. 390–400.

[12] G. L. Ramalho, D. S. Ferreira, A. G. Bianchi, C. M. Carneiro, F. N. Medeiros, and D. M. Ushizima, "Cell reconstruction under voronoi and enclosing ellipses from 3D microscopy," *IEEE ISBI Second Overlapping Cervical Cytology Image Segmentation Challenge*, pp. 3–4, 2015.

[13] H. Phoulady, D. Goldgof, L. Hall, and P. Mouton, "An approach for overlapping cell segmentation in multi-layer cervical cell volumes," *IEEE ISBI Second Overlapping Cervical Cytology Image Segmentation Challenge*, 2015.

[14] ——, "A new approach to detect and segment overlapping cells in multi-layer cervical cell volume images," in *ISBI*. IEEE, 2016, pp. 201–204.

[15] H. Lee and J. Kim, "Segmentation of overlapping cervical cells in microscopic images with superpixel partitioning and cell-wise contour refinement," in *CVPR*, 2016, pp. 63–69.

[16] P. Kumar, S. Happy, S. Chatterjee, D. Sheet, and A. Routray, "An unsupervised approach for overlapping cervical cell cytoplasm segmentation," in *IECBES*. IEEE, 2016, pp. 106–109.

[17] A. Tareef, Y. Song, W. Cai, H. Huang, H. Chang, Y. Wang, M. Fulham, D. Feng, and M. Chen, "Automatic segmentation of overlapping cervical smear cells based on local distinctive features and guided shape deformation," *Neurocomp.*, vol. 221, pp. 94–107, 2017.

[18] A. Tareef, Y. Song, H. Huang, Y. Wang, D. Feng, M. Chen, and W. Cai, "Optimizing the cervix cytological examination based on deep learning and dynamic shape modeling," *Neurocomp.*, vol. 248, pp. 28–40, 2017.

[19] P. Bamford and B. Lovell, "Unsupervised cell nucleus segmentation with active contours," *Signal Processing*, vol. 71, no. 2, pp. 203–213, 1998.

[20] M. E. Plissiti, C. Nikou, and A. Charchanti, "Automated detection of cell nuclei in Pap smear images using morphological reconstruction and clustering," *IEEE Transactions on Information Technology in Biomedicine*, vol. 15, no. 2, pp. 233–241, 2011.

[21] ——, "Combining shape, texture and intensity features for cell nuclei extraction in Pap smear images," *Pattern Recognition Letters*, vol. 32, no. 6, pp. 838–853, 2011.

[22] C. Jung and C. Kim, "Segmenting clustered nuclei using H-minima transform-based marker extraction and contour parameterization," *IEEE Trans. Biomed. Eng.*, vol. 57, no. 10, pp. 2600–2604, 2010.

[23] M. Plissiti, C. Nikou, and A. Charchanti, "Watershed-based segmentation of cell nuclei boundaries in Pap smear images," in *IEEE International Conference on Information Technology and Applications in Biomedicine (ITAB)*. IEEE, 2010, pp. 1–4.

[24] C. Jung, C. Kim, S. W. Chae, and S. Oh, "Unsupervised segmentation of overlapped nuclei using Bayesian classification," *IEEE Trans. Biomed. Eng.*, vol. 57, no. 12, pp. 2825–2832, 2010.

[25] M. Hu, X. Ping, and Y. Ding, "Automated cell nucleus segmentation using improved snake," in *ICIP*, vol. 4. IEEE, 2004, pp. 2737–2740.

[26] M. E. Plissiti, C. Nikou, and A. Charchanti, "Accurate localization of cell nuclei in Pap smear images using gradient vector flow deformable models." in *BIOSIGNALS*, 2010, pp. 284–289.

[27] C. Bergmeir, M. García Silvente, and J. M. Benítez, "Segmentation of cervical cell nuclei in high-resolution microscopic images: A new algorithm and a web-based software framework," *Computer Methods and Programs in Biomedicine*, vol. 107, no. 3, pp. 497–512, 2012.

[28] M. E. Plissiti and C. Nikou, "Cell nuclei segmentation by learning a physically based deformable model," in *International Conference on Digital Signal Processing (DSP)*. IEEE, 2011, pp. 1–6.

[29] M. Plissiti, A. Charchanti, O. Krikoni, and D. Fotiadis, "Automated segmentation of cell nuclei in Pap smear images," in *IEEE International Special Topic Conference on Information Technology in Biomedicine*. Citeseer, 2006, pp. 26–28.

[30] C. Chen, W. Wang, J. A. Ozolek, and G. K. Rohde, "A flexible and robust approach for segmenting cell nuclei from 2D microscopy images using supervised learning and template matching," *Cytometry Part A*, vol. 83, no. 5, pp. 495–507, 2013.

[31] R. Saha, M. Bajger, and G. Lee, "Spatial shape constrained fuzzy c-means (FCM) clustering for nucleus segmentation in Pap smear images," in *DICTA*. IEEE, 2016, pp. 1–8.

[32] A. Kale and S. Aksoy, "Segmentation of cervical cell images," in *International Conference on Pattern Recognition (ICPR)*. IEEE, 2010, pp. 2399–2402.

[33] A. Gentav, S. Aksoy, and S. nder, "Unsupervised segmentation and classification of cervical cell images," *Pattern Recognition*, vol. 45, no. 12, pp. 4151–4168, 2012.

[34] C.-H. Lin, Y.-K. Chan, and C.-C. Chen, "Detection and segmentation of cervical cell cytoplast and nucleus," *International Journal of Imaging Systems and Technology*, vol. 19, no. 3, pp. 260–270, 2009.

[35] T. Chankong, N. Theera-Umpon, and S. Auephanwiriyakul, "Automatic cervical cell segmentation and classification in pap smears," *Computer Methods and Programs in Biomedicine*, vol. 113, no. 2, pp. 539–556, 2014.

[36] K. Li, Z. Lu, W. Liu, and J. Yin, "Cytoplasm and nucleus segmentation in cervical smear images using radiating GVF snake," *Pattern Recognition*, vol. 45, no. 4, pp. 1255–1264, 2012.

[37] J. Fan, R. Wang, S. Li, and C. Zhang, "Automated cervical cell image segmentation using level set based active contour model," in *International Conference on Control Automation Robotics & Vision (ICARCV)*. IEEE, 2012, pp. 877–882.

[38] S.-F. Yang-Mao, Y.-K. Chan, and Y.-P. Chu, "Edge enhancement nucleus and cytoplast contour detector of cervical smear images," *IEEE Transactions on Systems, Man, and Cybernetics, Part B (Cybernetics)*, vol. 38, no. 2, pp. 353–366, 2008.

[39] M. Guven and C. Cengizler, "Data cluster analysis-based classification of overlapping nuclei in pap smear samples," *BME online*, vol. 13, no. 1, p. 159, 2014.

[40] E. Bengtsson, O. Eriksson, J. Holmquist, T. Jarkrans, B. Nordin, and B. Stenkvist, "Segmentation of cervical cells: detection of overlapping cell nuclei," *Comput. Gr. Image Process.*, vol. 16, no. 4, pp. 382–394, 1981.

[41] N. Béliz-Osorio, J. Crespo, M. García-Rojo, A. Muñoz, and J. Azpiazu, "Cytology imaging segmentation using the locally constrained watershed transform," in *Mathematical Morphology and Its Applications to Image and Signal Processing*. Springer, 2011, pp. 429–438.

[42] Y. Song, L. Zhang, S. Chen, D. Ni, B. Lei, and T. Wang, "Accurate segmentation of cervical cytoplasm and nuclei based on multiscale convolutional network and graph partitioning," *IEEE Trans. Biomed. Eng.*, vol. 62, no. 10, pp. 2421–2433, 2015.

[43] L. Zhang, H. Kong, C. T. Chin, S. Liu, Z. Chen, T. Wang, and S. Chen, "Segmentation of cytoplasm and nuclei of abnormal cells in cervical cytology using global and local graph cuts," *Computerized Medical Imaging and Graphics*, vol. 38, no. 5, pp. 369–380, 2014.

[44] S. Kaur and J. Sahambi, "Curvelet initialized level set cell segmentation for touching cells in low contrast images," *Computerized Medical Imaging and Graphics*, vol. 49, pp. 46–57, 2016.

[45] Z. Lu, G. Carneiro, and A. P. Bradley, "Automated nucleus and cytoplasm segmentation of overlapping cervical cells," in *MICCAI*. Springer, 2013, pp. 452–460.

[46] L. Vincent and P. Soille, "Watersheds in digital spaces: an efficient

algorithm based on immersion simulations," *IEEE Trans. Pattern Anal. Mach. Intell.*, vol. 13, no. 6, pp. 583–598, 1991.

[47] J. Yan, B. Zhao, L. Wang, A. Zelenetz, and L. H. Schwartz, "Marker-controlled watershed for lymphoma segmentation in sequential ct images," *Med. Phys.*, vol. 33, no. 7, pp. 2452–2460, 2006.

[48] G. Zack, W. Rogers, and S. Latt, "Automatic measurement of sister chromatid exchange frequency." *J. Histochemistry & Cytochemistry*, vol. 25, no. 7, pp. 741–753, 1977.

[49] R. Achanta, A. Shaji, K. Smith, A. Lucchi, P. Fua, and S. Susstrunk, "SLIC superpixels compared to state-of-the-art superpixel methods," *IEEE Trans. Pattern Anal. Mach. Intell.*, vol. 34, no. 11, pp. 2274–2282, 2012.

[50] J. Cheng, J. C. Rajapakse *et al.*, "Segmentation of clustered nuclei with shape markers and marking function," *IEEE Trans. Biomed. Eng.*, vol. 56, no. 3, pp. 741–748, 2009.

[51] S. Arslan, T. Ersahin, R. Cetin-Atalay, and C. Gunduz-Demir, "Attributed relational graphs for cell nucleus segmentation in fluorescence microscopy images," *IEEE Trans. Med. Imag.*, vol. 32, no. 6, pp. 1121–1131, 2013.

[52] P. Soille, *Morphological image analysis: principles and applications*. Springer-Verlag New York, Inc., 2003.

[53] K. F. Mulchrone and K. R. Choudhury, "Fitting an ellipse to an arbitrary shape: implications for strain analysis," *J. Structural Geology*, vol. 26, no. 1, pp. 143–153, 2004.

[54] K. Zuiderveld, "Contrast limited adaptive histogram equalization," in *Graphics Gems IV*. Academic Press Professional, Inc., 1994, pp. 474–485.

[55] T. F. Chan and L. A. Vese, "Active contours without edges," *IEEE Trans. Image Process.*, vol. 10, no. 2, pp. 266–277, 2001.

[56] Overlapping Cervical Cytology Image Segmentation Challenge-ISBI 2014, http://cs.adelaide.edu.au/ carneiro/isbi14_challenge/.

[57] Second Overlapping Cervical Cytology Image Segmentation Challenge-ISBI 2015, http://cs.adelaide.edu.au/ zhi/isbi15_challenge/.

[58] Z. Lu, G. Carneiro, A. Bradley, D. Ushizima, M. S. Nosrati, A. Bianchi, C. Carneiro, and G. Hamarneh, "Evaluation of three algorithms for the segmentation of overlapping cervical cells," *IEEE J. Biomed. Health Inform.*, vol. 21, no. 2, pp. 441–450, 2017.